JPE 15-4-14

http://dx.doi.org/10.6113/JPE.2015.15.4.1006
ISSN(Print): 1598-2092 / ISSN(Online): 2093-4718

Finite Control Set Model Predictive Control of AC/DC Matrix Converter for Grid-Connected Battery Energy Storage Application

Bo Feng[†] and Hua Lin[*]

[†*]State Key Laboratory of Advanced Electromagnetic Engineering and Technology,
School of Electrical and Electronic Engineering, Huazhong University of Science and Technology, Wuhan, China

Abstract

This paper presents a finite control set model predictive control (FCS-MPC) strategy for the AC/DC matrix converter used in grid-connected battery energy storage system (BESS). First, to control the grid current properly, the DC current is also included in the cost function because of input and output direct coupling. The DC current reference is generated based on the dynamic relationship of the two currents, so the grid current gains improved transient state performance. Furthermore, the steady state error is reduced by adding a closed-loop. Second, a Luenberger observer is adopted to detect the AC input voltage instead of sensors, so the cost is reduced and the reliability can be enhanced. Third, a switching state pre-selection method that only needs to evaluate half of the active switching states is presented, with the advantages of shorter calculation time, no high dv/dt at the DC terminal, and less switching loss. The robustness under grid voltage distortion and parameter sensibility are discussed as well. Simulation and experimental results confirm the good performance of the proposed scheme for battery charging and discharging control.

Key words: AC/DC matrix converter, Battery energy storage system, Model predictive control

I. INTRODUCTION

With the spring up of renewable energy generation and smart grid, the energy storage technology, especially the battery energy storage system (BESS), has found increased applications. Voltage source converter (VSC) is widely used as an interface between grid and battery. However, the battery usually has a lower voltage than the grid. Therefore, a large number of battery cells must be connected in series or an additional bi-directional DC/DC converter is required to achieve voltage level matching [1], [2].

AC/DC matrix converter is a novel converter topology derived from the well-known AC/AC matrix converter [3], [4]. It has been studied in several applications, such as DC motor drive [5], power supply [6], and battery charger [7], [8]. It inherits many advantages from the AC/AC matrix converter, such as: 1) compact structure without bulky electrolytic capacitor, 2) sinusoidal AC current and controllable power factor, and 3) four-quadrant operation capability [9]-[11]. More importantly, it is intrinsically a buck converter and features a tight DC voltage regulation in a wide range. Thus, it is an attractive alternative to the VSC-based topologies.

In grid-connected BESS application, grid current is the primary control objective, while the reported studies on AC/DC matrix converter mainly focused on DC side control. Traditionally, the converter is controlled with the aid of a modulator. In [7] and [8], space vector modulation (SVM) is utilized. A dual-loop control scheme with outer DC voltage and inner DC current loops is used. The AC input current is set to be in phase with the grid voltage, while its amplitude is indirectly controlled. In [12], the DC voltage controller sets the *d*-axis AC input current reference and then the AC input current is directly controlled using a one-cycle control strategy without a modulator. In these strategies, the AC side performance greatly depends on the DC side linear

Manuscript received Oct. 12, 2014; accepted Mar. 06, 2015
Recommended for publication by Associate Editor Marian P. Kazmierkowski.
[†]Corresponding Author: fengbohust@163.com
Tel: +86-027-87543658, Huazhong Univ. of Science and Technology
[*]State Key Laboratory of Advanced Electromagnetic Engineering and Technology, School of Electrical and Electronic Engineering, Huazhong University of Science and Technology, China

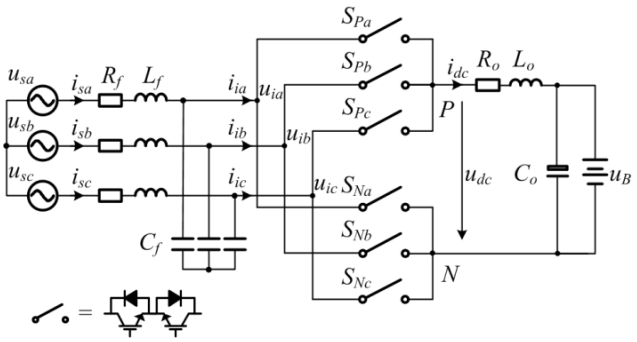

Fig. 1. AC/DC matrix converter circuit.

controllers. Moreover, the AC input current is controlled rather than the grid current. Because of the presence of AC side filter capacitors, the amplitude and phase of the grid current cannot be controlled precisely.

Finite control set model predictive control (FCS-MPC, hereafter referred to as MPC) provides a way to regulate the grid current directly and quickly. It takes advantage of the discrete and nonlinear nature of switching power converters and proves to be a simple and effective alternative to traditional control schemes. It offers many benefits, such as fast dynamic response, easy inclusion of nonlinearities and constraints, and does not need a modulator [13], [14]. The MPC scheme uses a discrete model to predict the system behavior in every possible switching state. Then, the predicted values are used to evaluate a cost function that can be customized flexibly according to specific requirements. Finally, the switching state that leads to the minimum cost function is selected and applied in the next sampling instant.

The MPC strategies for AC/AC matrix converter and current source rectifier can be used as references for the control of the AC/DC matrix converter because these converters have similar structures. Among them, the MPC with imposed sinusoidal source current shows excellent currents at both output and input, which is very attractive [15]-[17]. In this method, besides the load current control, the source current is also forced to follow a sinusoidal waveform. The source current reference is obtained from the load current reference according to the steady state input and output power balance. However, the difference between the dynamic responses of the two currents is not considered. In addition, the generated reference relates to the converter efficiency that varies with the operation condition. The accuracy of this parameter will affect the steady state tracking error, as analyzed in a study on predictive controlled back-to-back converter [18].

MPC requires the information of both AC source and input voltages [15]-[17], whereas the conventional control schemes only need either of the voltages. Voltage sensors increase the system size and cost and raises the risk of control failure caused by sensor malfunction. For the voltage source inverter, an observer can be used to estimate the load current without increasing the number of sensors [19]. However, using an observer to estimate the AC input voltage in an AC/DC matrix converter has not been mentioned in literature.

Evaluating all the switching states will lead to several problems. First, the calculation process is time-consuming, which limits the sampling frequency and eventually degrades the control performance. Many methods have been proposed to simplify the MPC algorithm for two- and multi-level VSCs [20]-[22]. Second, the output side will bear too large *dv*/*dt* [23]. Third, the switching loss may be higher. Therefore, discussing the switching state selection method for the MPC of the AC/DC matrix converter is worthwhile.

The contribution of this paper is the MPC implementation on an AC/DC matrix converter for grid-connected BESS application. To address the above issues, three aspects are investigated. First, the grid and DC currents are both controlled using a single cost function. The reference of the DC current is generated considering the transient state relationship of the two currents, and a proportional-integral (PI) controller is added to compensate for the steady state error. Second, the methods to estimate the AC input voltage are discussed. A Luenberger observer, which reduces cost and enhances reliability, is adopted. Third, to reduce the calculation amount and switching loss, as well as eliminate high *dv*/*dt*, a switching states pre-selection method based on the input current sector is proposed. Moreover, the robustness under grid voltage distortion and parameter sensitivity are discussed through simulation. Experiments are carried out on an AC/DC matrix converter prototype with a battery load to evaluate the proposed methods.

II. Predictive Model

The AC/DC matrix converter circuit is shown in Fig. 1. The power stage consists of six bidirectional switches, and each switch is implemented using two insulated gate bipolar transistors (IGBTs) with freewheeling diodes in common emitter configuration. The AC side *LC* filter is generally required for matrix converters to prevent over voltage and attenuate high-frequency input current harmonics. Subscripts "*s*," "*i*," and "*dc*" denote grid side, AC input side, and DC side quantities, respectively. R_f, L_f, and C_f are the AC filter parameters. R_o, L_o, and C_o are the DC filter parameters. S_{ij} (i = P, N and j = a, b, c) are the switching signals, S_{ij} = 1, 0. Complying with the restriction that no short-circuit at the AC side and no open-circuit at the DC side, nine switching states are feasible in the AC/DC matrix converter.

The AC input currents and the DC voltage are derived as

$$\begin{bmatrix} i_{ia} \\ i_{ib} \\ i_{ic} \end{bmatrix} = \begin{bmatrix} S_{Pa} - S_{Na} \\ S_{Pb} - S_{Nb} \\ S_{Pc} - S_{Nc} \end{bmatrix} i_{dc} \tag{1}$$

$$u_{dc} = (S_{Pa} - S_{Na})u_{ia} + (S_{Pb} - S_{Nb})u_{ib} + (S_{Pc} - S_{Nc})u_{ic} \tag{2}$$

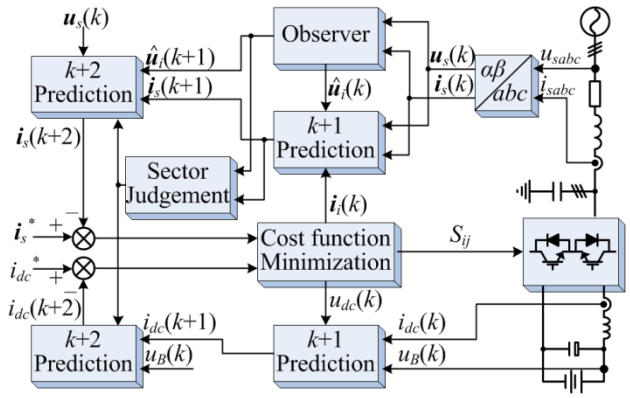

Fig. 2. Control scheme of the proposed MPC strategy.

To reduce the amount of calculation, the MPC algorithm is implemented in the stationary $\alpha\beta$ frame. At the AC side, the second order filter dynamics can be described as

$$\boldsymbol{u}_s = R_f \boldsymbol{i}_s + L_f \frac{d\boldsymbol{i}_s}{dt} + \boldsymbol{u}_i \tag{3}$$

$$\boldsymbol{i}_s = \boldsymbol{i}_i + C_f \frac{d\boldsymbol{u}_i}{dt} \tag{4}$$

where the bold letters represent the matrix of α- and β-components.

The state-space representation of the continuous-time system is

$$\dot{\boldsymbol{x}} = \underbrace{\begin{bmatrix} -R_f/L_f & -1/L_f \\ 1/C_f & 0 \end{bmatrix}}_{\mathbf{A}} \boldsymbol{x} + \underbrace{\begin{bmatrix} 0 & 1/L_f \\ -1/C_f & 0 \end{bmatrix}}_{\mathbf{B}} \boldsymbol{u} \tag{5}$$

with $\boldsymbol{x} = \begin{bmatrix} \boldsymbol{i}_s & \boldsymbol{u}_i \end{bmatrix}^T$ and $\boldsymbol{u} = \begin{bmatrix} \boldsymbol{i}_i & \boldsymbol{u}_s \end{bmatrix}^T$.

Considering the sampling period T_s, the discrete-time model of the AC side filter can be obtained by

$$\boldsymbol{x}(k+1) = \mathbf{A}_d \boldsymbol{x}(k) + \mathbf{B}_d \boldsymbol{u}(k) \tag{6}$$

where $\mathbf{A}_d = e^{\mathbf{A}T_s}$ and $\mathbf{B}_d = \int_0^{T_s} e^{\mathbf{A}(T_s-\tau)} \mathbf{B} d\tau$.

According to Equ. (6), the grid current $\boldsymbol{i}_s$ at time instant k + 1 is expressed as

$$\begin{aligned} \boldsymbol{i}_s(k+1) = {} & \mathbf{A}_d(1,1)\boldsymbol{i}_s(k) + \mathbf{A}_d(1,2)\boldsymbol{u}_i(k) \\ & + \mathbf{B}_d(1,1)\boldsymbol{i}_i(k) + \mathbf{B}_d(1,2)\boldsymbol{u}_s(k) \end{aligned} \tag{7}$$

where $\mathbf{\Lambda}$(m, n) is the (m, n) element of matrix $\mathbf{\Lambda}$.

To avoid the performance deterioration caused by the delay effect in digital implementation, a two-step-ahead prediction method [13] is adopted. By shifting Equ. (7) one step forward, the grid current at time instant k + 2 is obtained by Equ. (8). For simplicity, $\boldsymbol{u}_s(k+1) \approx \boldsymbol{u}_s(k)$ because of its small change in one sampling period.

$$\begin{aligned} \boldsymbol{i}_s(k+2) = {} & \mathbf{A}_d(1,1)\boldsymbol{i}_s(k+1) + \mathbf{A}_d(1,2)\boldsymbol{u}_i(k+1) \\ & + \mathbf{B}_d(1,1)\boldsymbol{i}_i(k+1) + \mathbf{B}_d(1,2)\boldsymbol{u}_s(k) \end{aligned} \tag{8}$$

The DC side behavior can be described by Equ. (9). Because only high-frequency currents flow through the DC filter capacitor, this capacitor is ignored in the modeling.

$$u_{dc} = L_o \frac{di_{dc}}{dt} + R_o i_{dc} + u_B \tag{9}$$

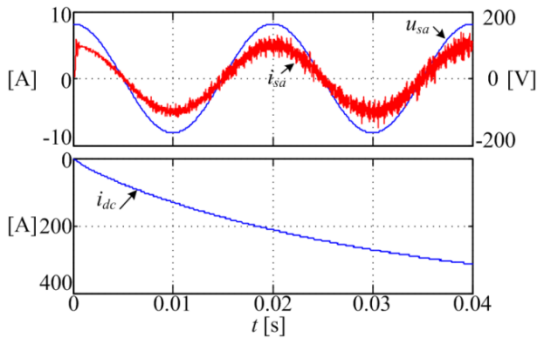

Fig. 3. Simulation waveforms with only grid current control.

Because Equ. (9) is a first-order system, the DC current can be predicted simply using the forward Euler approximation as Equs. (10) and (11), where $u_B(k+1) \approx u_B(k)$.

$$i_{dc}(k+1) = \left(1 - \frac{R_o T_s}{L_o}\right) i_{dc}(k) + \frac{T_s}{L_o}\left[u_{dc}(k) - u_B(k)\right] \tag{10}$$

$$i_{dc}(k+2) = \left(1 - \frac{R_o T_s}{L_o}\right) i_{dc}(k+1) + \frac{T_s}{L_o}\left[u_{dc}(k+1) - u_B(k)\right] \tag{11}$$

Fig. 2 provides an overview of the proposed MPC strategy. Details of the cost function design, AC input voltage estimation, and switching states pre-selection based on sector judgment are discussed in the following sections.

III. Cost Function Design

A. Cost Function

The goal of a grid-connected BESS is to control the grid current according to the grid command. However, in an AC/DC matrix converter, the AC and DC sides are directly connected through bidirectional switches without energy storage capability, so they should be controlled together. Fig. 3 presents the simulation waveforms of the predictive control with a cost function involving only the grid current. Though the grid current follows a 5A reference, the DC current is in reverse and far beyond the limit.

Thanks to the flexibility of controlling multiple variables in MPC, the grid and DC currents can be controlled simultaneously by including them in a single cost function as follows:

$$g = \frac{\left(i_{s\alpha}^* - i_{s\alpha}\right)^2 + \left(i_{s\beta}^* - i_{s\beta}\right)^2}{I_s^2} + \lambda \frac{\left(i_{dc}^* - i_{dc}\right)^2}{i_{dc}^2} \tag{12}$$

where I_s is the grid current amplitude (negative I_s corresponds to the discharging mode) and λ is the weighting factor, which assigns more priority to one variable or another.

Usually, λ is determined using repetitive simulations to achieve satisfactory results for the control objective. The total harmonic distortion (THD) and the amplitude error I_{s_err} of the grid current are used to evaluate λ because this paper aims at grid side control. Fig. 4 shows the simulation results of the

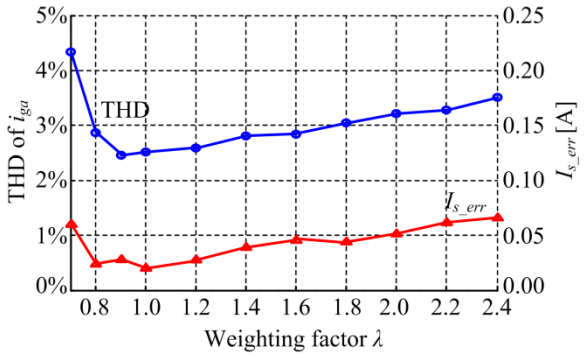

Fig. 4. Simulation results of grid current THD and amplitude error I_{s_err} in terms of weighting factor λ.

two indices in terms of λ, under a –5A grid current. Obviously, a smaller λ leads to a better grid current because the grid current is assigned more importance. However, when λ is less than 0.8, the grid current quality deteriorated quickly. This is because the DC current control is greatly weakened, which in turn affects the grid current. A too small λ will even cause instability. Considering the grid current performance and system stability, λ is set to 1.

According to the AC and DC side power balance, the ratio of grid current amplitude to DC current is equal to the ratio of battery voltage to grid voltage amplitude U_s. Then, the cost function can be simplified into Equ. (13). The coefficient of the DC term is approximately constant because the variations on the grid and battery voltages are very small.

$$g=\left(i_{s\alpha}^{*}-i_{s\alpha}\right)^{2}+\left(i_{s\beta}^{*}-i_{s\beta}\right)^{2}+\left(\frac{2u_B}{3U_s}\right)^{2}\left(i_{dc}^{*}-i_{dc}\right)^{2} \tag{13}$$

B. DC Current Reference Generation

A problem that arises when applying the cost function is the unavoidable coupling of the grid and DC currents. To control the grid current to track the grid command properly, the DC current reference cannot be arbitrarily chosen. Therefore, the generation of this reference is a key issue.

1) Method 1: The MPC with imposed sinusoidal source current method offers an effective method to calculate the AC source current reference from the desired AC or DC load current based on active power balance. This idea is also applicable in this paper, except that the grid current becomes the primary target and the DC current the subordinate control objective.

The accurate AC input side active power model is

$$p_i=\frac{3}{2}\left(u_{i\alpha}i_{i\alpha}+u_{i\beta}i_{i\beta}\right)=\frac{3}{2}I_s\left(1-2\omega_s^2L_fC_f\right)\left(U_s-R_fI_s\right) \tag{14}$$

At the DC output side, the active power is expressed as

$$p_o=R_oi_{dc}^2+u_Bi_{dc} \tag{15}$$

Considering the converter loss in a real system, the relationship between the input and output active power is

$$p_i=\eta p_o \tag{16}$$

where η is the efficiency in charging mode or the reciprocal of the efficiency in discharging mode.

From Equs. (14)–(16), the DC current reference i_{dc}^{*} is determined by the amplitude of grid current reference I_s^{*} as

$$i_{dc}^{*}=\sqrt{\left(\frac{u_B}{2R_o}\right)^2+\frac{3A\eta I_s^{*}\left(U_s-R_fI_s^{*}\right)}{2R_o}}-\frac{u_B}{2R_o} \tag{17}$$

with $A=1-8\omega_s^2L_fC_f$.

Equ. (17) only considers the steady state relationship of the two currents and ignores their dynamic behaviors, thus a step change in I_s^{*} will immediately generate a step change in i_{dc}^{*}. Using MPC, fast regulation of DC current is possible. However, the difference between the AC and DC side filter parameters indicates that the DC current essentially has a much slower dynamic response than the grid current. A sudden change in the DC current may incur a large overshoot or undershoot in the grid current. Therefore, forcing both currents to track simultaneous step-changed references is inappropriate. In fact, the change rate of i_{dc}^{*} should be limited.

Moreover, the obtained reference relies on accurate system parameters, especially on the converter efficiency. η varies with the operation condition (power level, charging or discharging, and so on) and its value should be adjusted empirically, which causes inconvenience in practical implementation. The mismatch of η will lead to inaccurate i_{dc}^{*} and finally affect the steady state tracking error of the grid current.

2) Method 2: The PI control enables the perfect tracking of constant reference, so the DC current reference can also be obtained using a PI control loop. Then, the steady state error caused by inaccurate efficiency parameter is eliminated.

The DC current reference can be expressed as

$$i_{dc}^{*}=\left(k_p+k_i/s\right)\left(I_s^{*}-I_s\right) \tag{18}$$

where k_p and k_i are the PI parameters.

Compared with Method 1, the dynamics of i_{dc}^{*} is greatly reduced because i_{dc}^{*} is completely determined by the error of grid current amplitude. Besides, tuning the PI parameters is a difficult task.

3) Method 3: To address the transient and steady state issues in Method 1 well, a novel strategy is proposed.

The AC filter has much faster dynamics than the DC filter, so the AC side dynamics can be neglected. Then, the following equation is established:

$$\frac{3}{2}U_sI_s=L_o\frac{di_{dc}}{dt}i_{dc}+u_Bi_{dc} \tag{19}$$

Applying a small-signal perturbation to Equ. (19), the transfer function from the grid current to the DC current is obtained by:

$$\frac{i_{dc}(s)}{I_s(s)}=\frac{3U_s}{2u_B}\frac{1}{\frac{L_oI_{dc}}{u_B}s+1} \tag{20}$$

where I_{dc} is the DC current at the operating point.

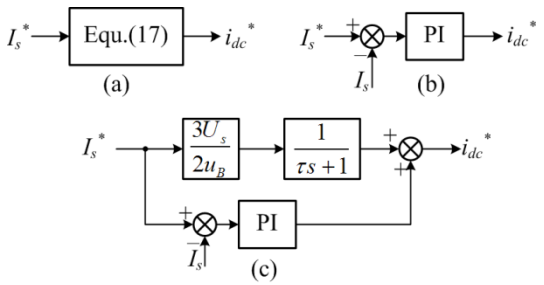

Fig. 5. DC current reference generation. (a) Method 1. (b) Method 2. (c) Method 3.

Equ. (20) indicates the transient state relationship of the two currents, that is, the change in i_{dc} lags behind the change in I_s. This should be considered when generating i_{dc}^*.

Moreover, i_{dc}^* is still derived in an open-loop manner like Method 1, thus also faces the steady state error problem. In view of this, a PI closed-loop is added as a supplement.

The DC current reference is finally expressed as

$$i_{dc}^* = \frac{3U_s}{2u_B}\frac{1}{\tau s+1}I_s^* + \left(k_p + k_i/s\right)\left(I_s^* - I_s\right) \tag{21}$$

where $\tau = L_o I_{dc}/u_B$.

Fig. 5 shows the DC current reference generation Methods 1–3. In Method 3, i_{dc}^* consists of two parts: the inertia term directly obtained from I_s^* and the PI term related to the actual error $I_s^* - I_s$. The inertia term, which is also a feed-forward of the grid current, plays the dominant role in both transient and steady states. By introducing $1/(\tau s + 1)$, the change rate of i_{dc}^* is limited, thus the overshoot of the grid current in transient state is reduced compared with that in Method 1. The PI parameters can be much smaller than those in Method 2 because the PI term is only utlized to deal with the tracking error in the steady state.

IV. AC Input Voltage Estimation

According to Equ. (8), among all the variables involved in predicting $\boldsymbol{i}_s(k+2)$, $\boldsymbol{u}_s(k)$ is needed for synchronization and $\boldsymbol{i}_s(k)$ is the control objective, thus the two variables should be measured. $\boldsymbol{i}_i(k)$ cannot be measured but can be calculated using the optimal switching state calculated in the last time instant, and $\boldsymbol{i}_i(k+1)$ relates to the optimal switching state for the next time instant. The input voltage can be measured. However, $\boldsymbol{u}_i(k)$ and $\boldsymbol{u}_i(k+1)$ are estimated to prevent increasing the number of sensors.

A simple way to estimate the AC input voltage is using the derivative Equ. (3). The AC input voltage at time instant k can be calculated as

$$\hat{\boldsymbol{u}}_i(k) = \boldsymbol{u}_s(k) - \left(R_f + \frac{L_f}{T_s}\right)\boldsymbol{i}_s(k) + \frac{L_f}{T_s}\boldsymbol{i}_s(k-1) \tag{22}$$

where "^" indicates an estimated value.

Then, the future AC input voltage can be derived using a simple extrapolation of the past estimated values as follow.

$$\hat{\boldsymbol{u}}_i(k+1) = 2\hat{\boldsymbol{u}}_i(k) - \hat{\boldsymbol{u}}_i(k-1) \tag{23}$$

However, this approach operates in an open-loop manner and is very sensitive to measurement noises because of the use of grid current derivation. Therefore, the method using a closed-loop observer is preferred.

The Luenberger observer uses the system model to predict the system state and then feeds back the difference between the measured and estimated output and corrects the model with this error signal to minimize the divergence between the model and the actual system. It can correct the model inaccuracy, eliminate the disturbance effect and noise, and has high reliability. Moreover, it presents a predictive nature so that a measurement at time instant k results in an observation of the state variables valid in time instant $k + 1$, and this is exactly what the two-step-ahead prediction needs.

Suppose the system output is the grid current,

$$\boldsymbol{y} = \underbrace{\begin{bmatrix}1 & 0\end{bmatrix}}_{\mathbf{C}}\boldsymbol{x} \tag{24}$$

The full-order observer is used to estimate the state vector $\boldsymbol{x}$. It consists of an open-loop model of the system and a correcting term related to the measured output. The observer dynamics can be represented by

$$\frac{d\hat{\boldsymbol{x}}}{dt} = \mathbf{A}\hat{\boldsymbol{x}} + \mathbf{B}\boldsymbol{u} + \mathbf{G}\left(\boldsymbol{y} - \hat{\boldsymbol{y}}\right) = \left(\mathbf{A}\text{-}\mathbf{GC}\right)\hat{\boldsymbol{x}} + \mathbf{B}\boldsymbol{u} + \mathbf{G}\boldsymbol{y} \tag{25}$$

where $\hat{\boldsymbol{y}} = \mathbf{C}\hat{\boldsymbol{x}}$ and $\mathbf{G} = \begin{bmatrix}h_1 & h_2\end{bmatrix}^T$ is the gain matrix.

The error vector of the observer is defined as $\tilde{\boldsymbol{x}} = \boldsymbol{x} - \hat{\boldsymbol{x}}$, thus its dynamics can be expressed as

$$\frac{d\tilde{\boldsymbol{x}}}{dt} = \left(\mathbf{A}\text{-}\mathbf{GC}\right)\tilde{\boldsymbol{x}} \tag{26}$$

To make the observer error converge to zero with time for any initial value, the observer gain matrix should be selected such that **A-GC** is asymptotically stable. In other words, all the eigenvalues of **A-GC** should have negative real parts. The characteristic equation of the system is

$$\det\left[s\mathbf{I} - \left(\mathbf{A}\text{-}\mathbf{GC}\right)\right] = s^2 + \frac{h_1 L_f + R_f}{L_f}s - \frac{h_2 C_f - 1}{L_f C_f} = 0 \tag{27}$$

The gain matrix can be determined by applying the pole placement method. Suppose the observer has a pair of conjugate complex poles $a \pm jb$, then the desired characteristic equation can be expressed as

$$(s - a - jb)(s - a + jb) = s^2 - 2as + a^2 + b^2 = 0 \tag{28}$$

Equs. (27) and (28) should be identical, and the elements of **G** can be obtained by matching the coefficients of each power of s as follows:

$$\begin{aligned} h_1 &= -2a - R_f/L_f \\ h_2 &= -L_f\left(a^2 + b^2\right) + 1/C_f \end{aligned} \tag{29}$$

A-GC determines the observer dynamics. The gain matrix **G** should be designed such that the observer poles are farther from the imaginary axis than the original system. If the

observer poles are closer to the imaginary axis, obtaining the actual value of the state variable will take a long time, whereas too far away from the imaginary axis, the system will be very sensitive to the noises and might be unstable. Therefore, a compromise should be made between bandwidth and noise rejection.

The discrete form of the observer is

$$\hat{\boldsymbol{x}}(k+1)=\mathbf{A}_o\hat{\boldsymbol{x}}(k)+\mathbf{B}_o\boldsymbol{u}(k)+\mathbf{G}_o\boldsymbol{y}(k) \tag{30}$$

where

$\mathbf{A}_o=e^{(\mathbf{A}-\mathbf{GC})T_s}$, $\mathbf{B}_o=\int_0^{T_s}e^{(\mathbf{A}-\mathbf{GC})(T_s-\tau)}\mathbf{B}d\tau$, and $\mathbf{G}_o=\int_0^{T_s}e^{(\mathbf{A}-\mathbf{GC})(T_s-\tau)}\mathbf{G}d\tau$.

Then, the AC input voltage at time $k+1$ can be calculated using the present measured grid voltages and currents.

V. Active Switching State Selection Method

The current prediction and cost function evaluation for all feasible switching states need a large amount of calculation, especially when multiple constrains are considered. If the calculations take too much time, a long sampling period should be used, which will degrade the control performance.

On the other hand, negative DC terminal voltage is allowed in an AC/DC matrix converter. For instance, in the charging mode, if the actual DC current is larger than the reference, the switching state corresponding to the negative DC terminal voltage may be selected because it can decrease the current quickly. However, jumping between positive and negative voltages will lead to large DC side dv/dt and high switching loss. The increase in switching loss results from the higher switching frequency because two commutations take place in one sampling period and higher switched voltage that is approximately proportional to the switching loss [24], [25].

Evaluating a subset instead of all the switching states will help shorten the calculation time. Furthermore, if the subset is selected properly, the negative DC terminal voltage can be avoided.

The input current sector concept in SVM is introduced. Take sector 1 as an example, where the sector angle θ lies in $(-\pi/6, \pi/6)$ [7]. Fig. 6(a) shows the AC input currents and the corresponding line voltages in charging mode. Sector 1 has three positive line voltages that can be applied at the DC terminal, namely, u_{iab}, u_{iac}, and u_{icb} in the first half of the sector $(-\pi/6, 0)$ and u_{iab}, u_{iac}, and u_{ibc} in the second half of the sector $(0, \pi/6)$. Thus, the optimization process needs to evaluate four active switching states *ab*, *ac*, *cb*, and *bc*, and the negative voltage still exists if *bc* is selected in the first half of the sector or *cb* is selected in the second half of the sector.

If the $\pi/3$ sector interval is shifted to the right by $\pi/6$, then

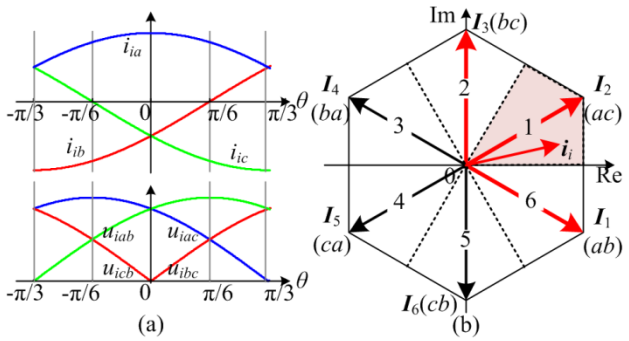

Fig. 6. AC input current sectors. (a) AC input currents and line voltages. (b) Proposed sector definition.

u_{iab}, u_{iac}, and u_{ibc} are all positive in the newly defined sector 1 $(0, \pi/3)$. As a result, the number of candidate active switching states is reduced to only three and the negative DC terminal voltage is eliminated. The new sector definition is shown in Fig. 6(b).

Ideally, the evaluation time of the active switching states can be reduced by half. However, judging the input current sector introduces extra computation; therefore, this procedure should also be optimized.

The actual AC input currents are PWM waveforms, so the fundamental component should be derived first.

For sinusoidal and balanced three-phase voltages, the following equations can be deduced [26]

$$\begin{aligned}\frac{du_{i\alpha}}{dt}&=-\omega_s u_{i\beta}\\ \frac{du_{i\beta}}{dt}&=\omega_s u_{i\alpha}\end{aligned} \tag{31}$$

Substituting Equ. (31) into Equ. (4), the fundamental AC input currents $i_{i\alpha}$ and $i_{i\beta}$ are derived by Equ. (32). $i_{i\alpha}$ and $i_{i\beta}$ can be readily calculated using the measured grid current and the estimated input voltage.

$$\begin{aligned}i_{i\alpha}&=i_{s\alpha}+\omega_s C_f u_{i\beta}\\ i_{i\beta}&=i_{s\beta}-\omega_s C_f u_{i\alpha}\end{aligned} \tag{32}$$

The conventional sector judgment method requires complex trigonometric and modulus manipulations [27]. Because the value of sector angle is not necessary for MPC, a simple approach without sector angle calculation is adequate.

Fig. 6(a) shows that in sector 1 $(0, \pi/3)$, the input phase currents have the following relationship.

$$i_{ia}\ge i_{ib},\quad i_{ib}\ge i_{ic} \tag{33}$$

By replacing i_{ia}, i_{ib}, and i_{ic} with $i_{i\alpha}$ and $i_{i\beta}$, Equ. (33) is rewritten as

$$i_{i\beta}\ge 0,\quad \sqrt{3}i_{i\alpha}-i_{i\beta}\ge 0,\quad -\sqrt{3}i_{i\alpha}-i_{i\beta}<0 \tag{34}$$

Similar relationships can be seen in the other sectors. P corresponds to the sector number and is defined as

$$P=\text{sign}(i_{i\beta})+2\text{sign}(\sqrt{3}i_{i\alpha}-i_{i\beta})+4\text{sign}(-\sqrt{3}i_{i\alpha}-i_{i\beta}) \tag{35}$$

where

$$\text{sign}(x)=\begin{cases}1, & x\ge 0\\ 0, & x<0\end{cases} \tag{36}$$

TABLE I
SECTOR JUDGEMENT AND ACTIVE SWITCHING STATE SUBSET

*P*0	*P*1	*P*2	*P*	Sector	Switching states
1	1	0	3	1	*ab*, *ac*, *bc*
1	0	0	1	2	*ac*, *bc*, *ba*
1	0	1	5	3	*bc*, *ba*, *ca*
0	0	1	4	4	*ba*, *ca*, *cb*
0	1	1	6	5	*ca*, *cb*, *ab*
0	1	0	2	6	*cb*, *ab*, *ac*

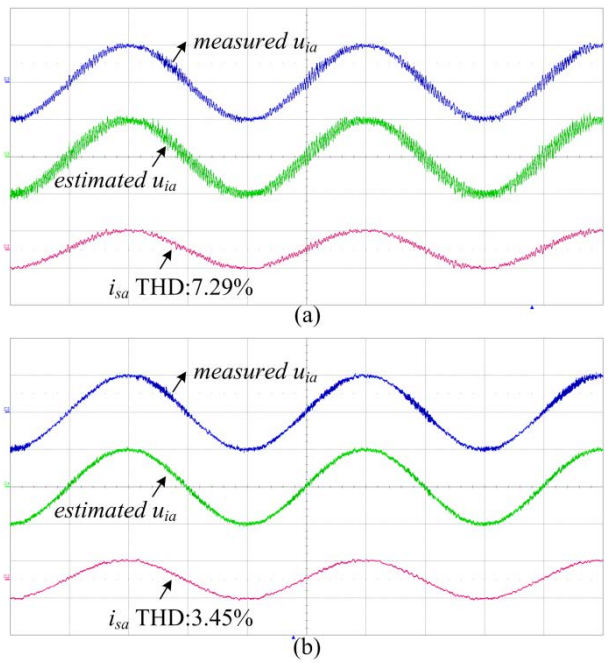

Fig. 7. Experimental waveforms using different AC input voltage estimation methods. (a) Derivative-based method. (b) Observer-based method. $u_{i\alpha}$ [160 V/div], i_{sa} [6 A/div], time [10 ms/div].

The sector number calculation and the candidate active switching states are listed in Table I, where $P0 = \text{sign}(i_{i\beta})$, $P1 = \text{sign}(\sqrt{3}i_{i\alpha} - i_{i\beta})$, and $P2 = \text{sign}(-\sqrt{3}i_{i\alpha} - i_{i\beta})$.

The sector number can be easily calculated using Equs. (32) and (35), and only a few addition and multiply operations, as well as a simple lookup table are used, which reduces the computational burden on the microprocessor.

VI. SIMULATION AND EXPERIMENTAL RESULTS

The proposed control methods are evaluated through Matlab simulation and experiment. Experimentally, the power stage is constructed with 12 discrete IGBTs of type IKW40N120. The MPC algorithm is executed in a DSP of type TMS320F28335, and the four-step current commutation is implemented using a FPGA of type EP2C8. The DC load is a 10 × 12 V/100 Ah lead-acid battery pack. Other system parameters are as follows: grid line voltage 200 Vrms/50 Hz; AC filter L_f = 1.2 mH, C_f = 10 μF, R_f = 0.1 Ω; DC filter L_o = 10 mH, C_o = 20 μF, R_o = 0.1 Ω; sampling period T_s = 20 μs.

A. Comparison of AC Input Voltage Estimation Methods

Fig. 7 shows the experimental waveforms using the simple estimation method based on derivative equation and with the Luenberger observer. The grid current is set to 3A charging. As observed, the derivative-based method results in a noisy input voltage that contains many harmonics, whereas the observer-based method obtains a clear input voltage with low THD. Because of the low pass filter effect of the observer, the estimated voltage presents less high frequency harmonics than the measured value, as shown in Fig. 7(b). The grid current waveforms indicate that the derivative-based method leads to poor control performance, whereas the observer-based method is suitable for MPC control.

B. Comparison of Active Switching State Selection Methods

Fig. 8 shows the experimental waveforms using the conventional six active switching states method and with the proposed three active switching states method. For fair comparison, the DC current references are all generated using Equ. (17) and η is empirically adjusted to 0.94 in charging mode and 1.11 in discharging mode to obtain a ±5A grid current. The figure shows that with the conventional method, many negative voltage pulses are generated at the DC side and the converter suffers from large *dv*/*dt*, especially in the discharging mode. By contrast, selecting among three active switching states strongly reduces the negative voltage pulses at the DC side and only slightly affects the current quality.

Table II lists the experimental data of –5A discharging. Compared with the conventional method, the proposed method reduces the evaluation time of the cost function by 35%. Moreover, the average switching frequency and the average switched voltage are reduced by 8% and 14%, respectively, which means a smaller switching loss.

In Method 1, η is set to 1 in both the charging and discharging modes. Like I_s^*, the generated i_{dc}^* changes in a stepped manner. The grid current presents a very large overshoot in the charging mode and undershoot in the discharging mode because of the drastic change in the DC current. On the other hand, because the actual efficiency is less than one, i_{dc}^* is not the accurate value that results in the desired grid current. Therefore, the grid current has a steady state amplitude error, and this problem is even worse in the discharging mode because of lower efficiency.

In Method 2, k_p = 0.4 and k_i = 800. As expected, the grid current amplitude error is eliminated. However, i_{dc}^* shows very different dynamic behaviors in the charging and discharging modes. i_{dc}^* takes a long time to reach the steady state in the charging mode. On the contrary, it responses fast and even oscillates in the discharging mode. Therefore, designing PI parameters suitable for both charging and discharging modes is difficult. The PI control is very sensitive to input noise and ripple, thus resulting in a

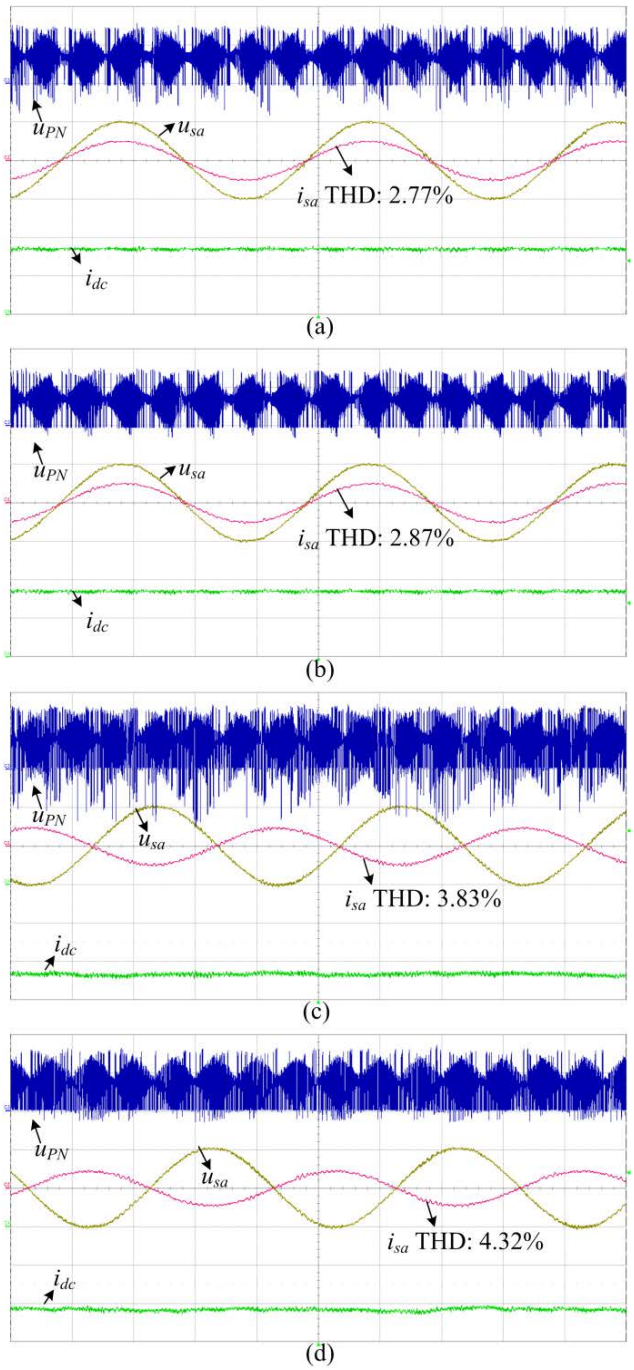

Fig. 8. Experimental waveforms using different active switching state selection methods. (a) Conventional method, charging. (b) Proposed method, charging. (c) Conventional method, discharging. (d) Proposed method, discharging. u_{PN} [200 V/div], u_{sa} [160 V/div], i_{sa} [10 A/div], i_{dc} [10 A/div], time [5 ms/div].

TABLE II
EXPERIMENTAL DATA WITH DIFFERENT ACTIVE SWITCHING STATE SELECTION METHODS

	Conventional	Proposed
Cost function calculation time	10 μs	6.5 μs
Average switching frequency	11.4 kHz	10.5 kHz
Average switched voltage	168 V	144 V

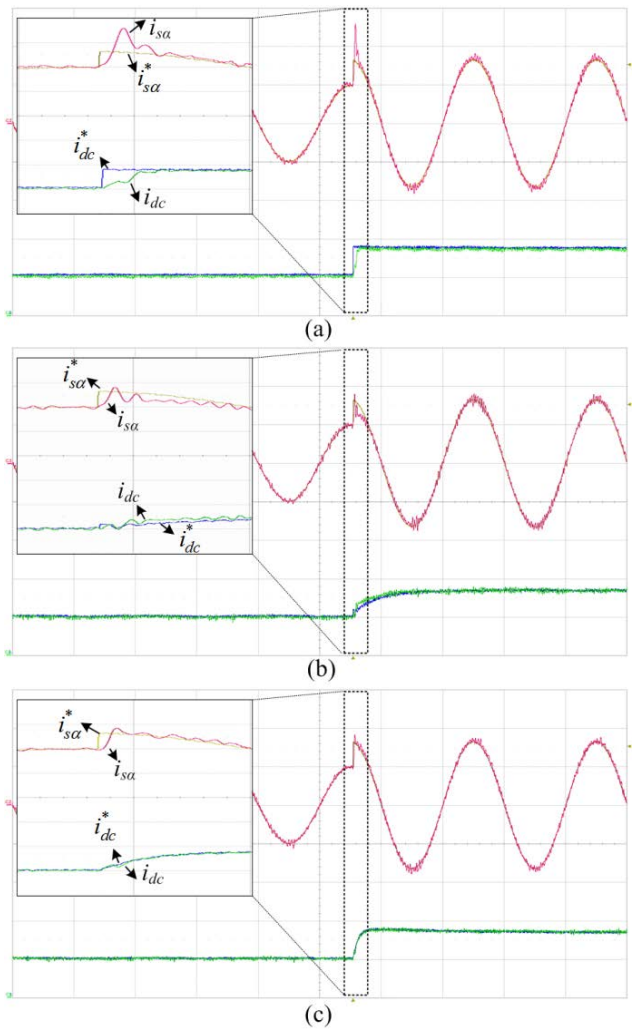

Fig. 9. Experimental waveforms using different DC current reference generation methods, charging. (a) Method 1. (b) Method 2. (c) Method 3. $i_{sa}{}^*$ and i_{sa} [3 A/div], $i_{dc}{}^*$ and i_{dc} [5 A/div], time [10 ms/div].

TABLE III
EXPERIMENTAL DATA WITH DIFFERENT DC CURRENT REFERENCE GENERATION METHODS

Method	5A charging		–5A discharging	
	I_s [A]	THD	I_s [A]	THD
1	5.18	3.02%	–3.91	4.11%
2	4.97	3.15%	–4.94	4.24%
3	5.02	2.87%	–4.95	3.84%

distorted $i_{dc}{}^*$. The DC current is forced to follow this non-ideal reference, so the grid current quality is damaged. As shown in Table III, the grid current has a higher THD.

C. Comparison of DC Current Reference Generation Methods

Figs. 9 and 10 show the experimental waveforms with different DC current reference generation methods. Table III lists the grid current amplitude and THD. The grid current changes from 3A to 5A and –3A to –5A, respectively.

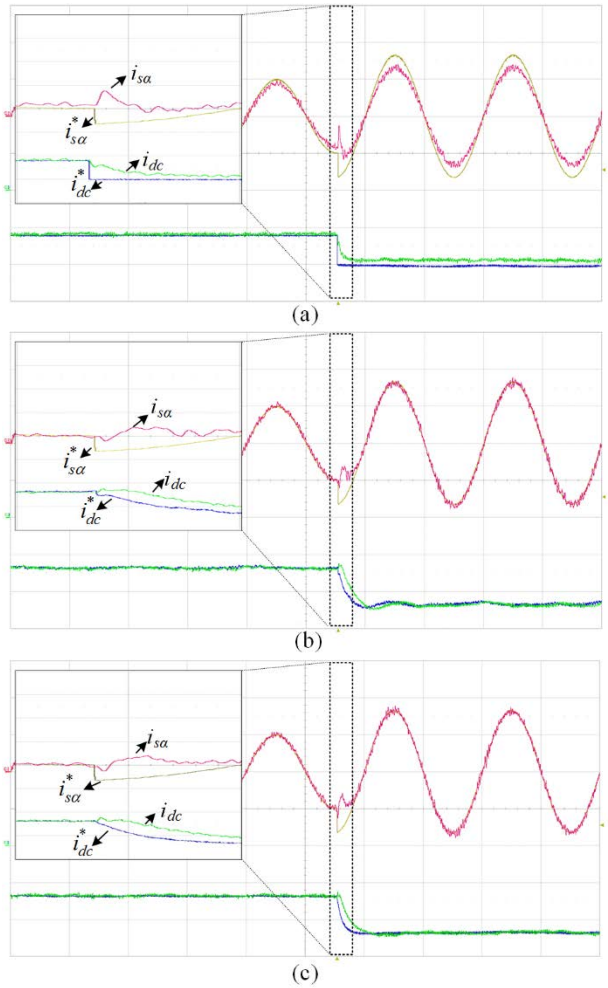

Fig. 10. Experimental waveforms using different DC current reference generation methods, discharging. (a) Method 1. (b) Method 2. (c) Method 3. $i_{sa}{}^*$ and i_{sa} [3 A/div], $i_{dc}{}^*$ and i_{dc} [5 A/div], time [10 ms/div].

In Method 3, because the inertia term considered the dynamic relationship of the two currents, the grid current tracks the reference very fast, but without the large overshoot, while the PI control (k_p = 0.1, k_i = 200) removes the amplitude error. PI has little effect on the quality of $i_{dc}{}^*$ and eventually the grid current THD because of the small PI parameters. In fact, because both currents are provided the correct references, they can be controlled more precisely.

D. Robustness under Grid Voltage Distortion

The actual grid usually contains 5th and 7th background harmonics, and this will be even worse for a weak grid. To demonstrate the robustness of the proposed control strategy on grid voltage distortion, simulations are carried out.

Fig. 11 shows the simulation waveforms. The grid voltage is set to have 5% and 3% of the 5th and 7th harmonics. Thanks to the high sampling frequency and fast dynamics of the Luenberger observer, the estimated input voltage tracks the actual value accurately despite of the distortion. The estimated value is one-step ahead because of the predictive

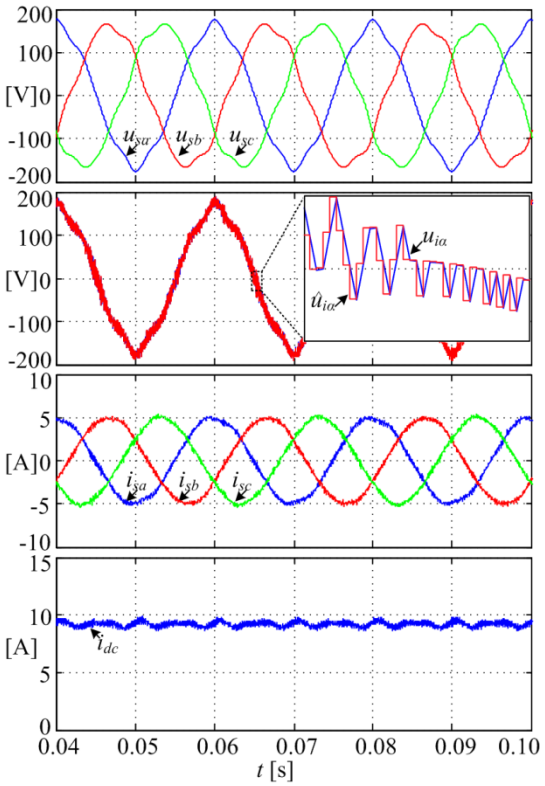

Fig. 11. Simulation waveforms under grid voltage distortion.

nature of the observer. With the MPC scheme, the grid current is directly forced to follow a sinusoidal reference, regardless of the grid voltage distortion. Therefore, the grid current waveforms are almost sinusoidal and the 5th and 7th harmonic components are only 1.4% and 0.45%, respectively. Obtaining ideal waveforms on both sides when the grid voltage is abnormal is impossible because of the direct coupling of the input and output in matrix converters. However, acceptable performances can be achieved because the cost function involves grid current tracking and DC current tracking at the same time.

E. Parameter Sensitivity

As shown in Equs. (8) and (11), the MPC requires information of the filter parameters to estimate and predict the future quantities. The mismatch of these parameters can degrade the control performance and affect the system stability. Therefore, investigating the control behavior under parameter changes is important. The inductor parasitic resistances R_f and R_o are very small and their modeling errors have negligible influence. The parameter variations of L_f, C_f, and L_o are analyzed through simulations. The actual filter parameters are nominal, while the values used in the predictive controller are considered to change from –30% to +30%.

Fig. 12 plots the grid current THD and the average switching frequency f_{avg}, and Fig. 13 shows the waveforms of the grid and DC currents. The system has similar behaviors

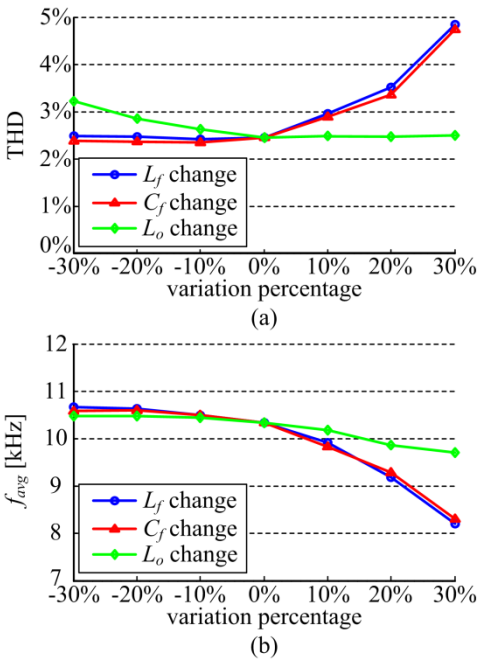

Fig. 12. Simulation results under model parameter variations. (a) Grid current THD. (b) Average switching frequency f_{avg}.

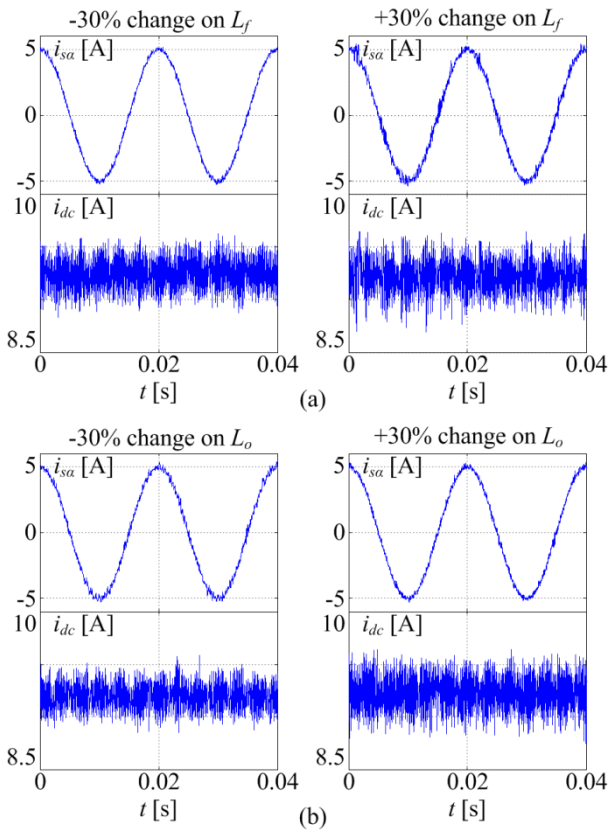

Fig. 13. Simulation waveforms under model parameter variations. (a) AC filter inductance L_f changes ±30%. (b) DC filter inductance L_o changes ±30%.

under the L_f and C_f variations. The underestimation of the two parameters has very small effects on the grid current, whereas the overestimation leads to worse grid current because when L_f and C_f are lower than the actual values, the coefficient of input current term $\mathbf{B}_d(1,1)$ in Equ. (8) becomes larger, then the prediction of grid current relies more on the input current that is directly associated with the selection of switching states. As a result, the switches operate more frequently for grid current reference tracking. Conversely, when L_f and C_f are higher than the actual values, the role of switching states on the grid current regulation is weakened. This can also be seen in the trends of the average switching frequency shown in Fig. 12(b). f_{avg} reduces greatly when L_f and C_f are overestimated, thus the grid current performance deteriorates significantly. The analysis of Equ. (11) indicates that the mismatch of L_o affects the DC current performance in a similar way. When L_o is higher than its actual value, the DC current is controlled more precisely. However, because of the tradeoff between grid current control and DC current control, the grid current quality is sacrificed. This is verified by Fig. 13(b), when L_o changes by –30%, the DC current ripple is smaller than that with the case when L_o changes by +30%, but the grid current contains more harmonics. Extreme parameter variations would severely degrade the control performance and even make the system unstable.

VII. Conclusion

The MPC scheme for AC/DC matrix converter applied in grid-connected BESS is discussed in this paper. To achieve good grid current regulation, the DC current is controlled as well. By using an improved DC current reference generation method, the grid current can track the reference quickly without a large overshoot or undershoot, and the steady state tracking error is reduced. The AC input voltage is estimated using a closed-loop observer, so the input voltage sensors are eliminated, which reduces the cost and enhances the system reliability. The number of active switching states for cost function evaluation is reduced by half, so the computation time is shortened, the switching loss is reduced, and large dv/dt at the DC terminal is avoided. The proposed MPC strategy is robust against grid voltage distortion. Parameter sensitivity is also investigated. Simulation and experimental results verify that the AC/DC matrix converter with the proposed strategy has good performance for battery charging and discharging control.

Acknowledgment

This work was supported by the National Basic Research Program of China under Award No. 2010CB227206.

References

[1] Z. Miao, L. Xu, V. R. Disfani, and L. Fan, “An SOC-based battery management system for microgrids,” *IEEE Trans. Smart Grid*, Vol. 5 , No. 2 , pp. 966-973, Mar. 2014.

[2] S. Inoue and H. Akagi, "A bidirectional DC-DC converter for an energy storage system with galvanic isolation," *IEEE Trans. Power Electron.*, Vol. 22 , No. 6 , pp. 2299-2306, Nov. 2007.

[3] D. G. Holmes and T. A. Lipo, "Implementation of a controlled rectifier using AC-AC matrix converter theory," *IEEE Trans. Power Electron.*, Vol. 7 , No. 1 , pp. 240-250, Jan. 1992.

[4] K. You, D. Xiao, M. F. Rahman, and M. N. Uddin, "Applying reduced general direct space vector modulation approach of AC/AC matrix converter theory to achieve direct power factor controlled three-phase AC-DC matrix rectifier," *IEEE Trans. Ind. Appl.*, Vol. 50 , No. 3 , pp. 2243-2257, May 2014.

[5] A. L. Julian and G. Oriti, "A novel clamp circuit for a regenerative rectifier using AC/AC matrix converter theory," *IEEE Trans. Ind. Appl.*, Vol. 41 , No. 1 , pp. 68-74, Jan. 2005.

[6] S. Ratanapanachote, J. C. Han, and P. N. Enjeti, "A digitally controlled switch mode power supply based on matrix converter," *IEEE Trans. Power Electron.*, Vol. 21 , No. 1 , pp. 124-130, Jan. 2006.

[7] R. Metidji, B. Metidji, and B. Mendil, "Design and implementation of a unity power factor fuzzy battery charger using an ultrasparse matrix rectifier," *IEEE Trans. Power Electron.*, Vol. 28 , No. 5 , pp. 2269-2276, May 2013.

[8] M. Su, H. Wang, Y. Sun, J. Yang, W. Xiong, and Y. Liu, "AC/DC matrix converter with an optimized modulation strategy for V2G applications," *IEEE Trans. Power Electron.*, Vol. 28 , No. 12 , pp. 5736-5745, Dec. 2013.

[9] P. W. Wheeler, J. Rodriguez, J. C. Clare, L. Empringham, and A. Weinstein, "Matrix converters: a technology review," *IEEE Trans. Ind. Electron.*, Vol. 49 , No. 2 , pp. 276-288, Apr. 2002.

[10] J. Rodriguez, M. Rivera, J. W. Kolar, and P. W. Wheeler, "A review of control and modulation methods for matrix converters," *IEEE Trans. Ind. Electron.*, Vol. 59 , No. 1 , pp. 58-70, Jan. 2012.

[11] L. Empringham, J. W. Kolar, J. Rodriguez, P. W. Wheeler, and J. C. Clare, "Technological issues and industrial application of matrix converters: a review," *IEEE Trans. Ind. Electron.*, Vol. 60 , No. 10 , pp. 4260-4271, Oct. 2013.

[12] X. Liu, Q. Zhang, and D. Hou, "One-cycle control strategy with active damping for an AC-DC matrix converter," *Journal of Power Electronics*, Vol. 14, No. 4, pp. 778-787, Jul. 2014.

[13] S. Kouro, P. Cortes, R. Vargas, U. Ammann, and J. Rodriguez, "Model predictive control – A simple and powerful method to control power converters," *IEEE Trans. Ind. Electron.*, Vol. 56 , No. 6 , pp. 1826-1838, Jun. 2009.

[14] J. Rodriguez, M. P. Kazmierkowski, J. R. Espinoza, P. Zanchetta, H. Abu-Rub, H. A. Young, and C. A. Rojas, "State of the art of finite control set model predictive control in power electronics," *IEEE Trans. Ind. Informat.*, Vol. 9 , No. 2 , pp. 1003-1016, May 2013.

[15] M. Rivera, J. Rodriguez, P. W. Wheeler, C. A. Rojas, A. Wilson, and J. R. Espinoza, "Control of a matrix converter with imposed sinusoidal source currents," *IEEE Trans. Ind. Electron.*, Vol. 59 , No. 4 , pp. 1939-1949, Apr. 2012.

[16] M. Rivera, C. Rojas, A. Wilson, J. Rodriguez, J. Espinoza, C. Baier, and J. Munoz, "Review of predictive control methods to improve the input current of an indirect matrix converter," *IET Power Electron.*, Vol. 7, No. 4, pp. 886-894, Apr. 2014.

[17] P. Zavala, M. Rivera, S. Kouro, J. Rodriguez, B. Wu, V. Yaramasu, C. Baier, J. Munoz, J. Espinoza, and P. Melin, "Predictive control of a current source rectifier with imposed sinusoidal input currents," in *Conf. IECON 2013*, pp. 5842-5847, 2013.

[18] Z. Zhang, F. Wang, T. Sun, J. Rodriguez, and R. Kennel, "FPGA based experimental investigation of a quasi-centralized DMPC scheme for a back-to-back converter," *IEEE Trans. Power Electron.*, to be published.

[19] P. Cortes, G. Ortiz, J. I. Yuz, J. Rodriguez, S. Vazquez, and L. G. Franquelo, "Model predictive control of an inverter with output LC filter for UPS applications," *IEEE Trans. Ind. Electron.*, Vol. 56 , No. 6 , pp. 1875-1883, Jun. 2009.

[20] P. Cortés, A. Wilson, S. Kouro, J. Rodriguez, and H. Abu-Rub, "Model predictive control of multilevel cascaded H-bridge inverters," *IEEE Trans. Ind. Electron.*, Vol. 57 , No. 8 , pp. 2691-2699, Aug. 2010.

[21] C. Xia, T. Liu, T. Shi, and Z. Song, "A simplified finite-control-set model-predictive control for power converters," *IEEE Trans. Ind. Inform.*, Vol. 10 , No. 2 , pp. 991-1002, May 2014.

[22] J. Hu, J. Zhu, G. Lei, G. Platt, and D. G. Dorrell, "Multi-objective model-predictive control for high-power converters," *IEEE Trans. Energy Convers.*, Vol. 28 , No. 3 , pp. 652-663, Sep. 2013.

[23] T. Shi, C. Zhang, Q. Geng, and C. Xia, "Improved model predictive control of three-level voltage source converter," *Electric Power Components and Systems*, Vol. 42 , No. 10 , pp. 1029-1038, Jun. 2014.

[24] R. Vargas, J. Rodriguez, C. A. Rojas, and M. Rivera, "Predictive control of an induction machine fed by a matrix converter with increased efficiency and reduced common-mode voltage," *IEEE Trans. Energy Convers.*, Vol. 29 , No. 2 , pp. 473-485, Jun. 2014.

[25] K. You and M. F. Rahman, "Analytical model of conduction and switching losses of matrix-Z-source converter," *Journal of Power Electronics*, Vol. 9 , No. 2 , pp. 275-287, Mar. 2009.

[26] S. A. Larrinaga, M. A. R. Vidal, E. Oyarbide, and J. R. T. Apraiz, "Predictive control strategy for DC/AC converters based on direct power control," *IEEE Trans. Ind. Electron.*, Vol. 54 , No. 3 , pp. 1261-1271, Jun. 2007.

[27] X. Wang, H. Lin, H. She, and B. Feng, "A research on space vector modulation strategy for matrix converter under abnormal input-voltage conditions," *IEEE Trans. Ind. Electron.*, Vol. 59 , No. 1 , pp. 93-104, Jan. 2012.

Bo Feng was born in Hubei, China, in 1987. He received a B.S. degree in Electrical Engineering and Automation in 2009 from the Huazhong University of Science and Technology (HUST), Wuhan, China, where he is currently working toward a Ph.D. degree in Power Electronics and Electrical Drive. His research interests include matrix converter and battery energy storage system.

Hua Lin was born in Wuhan, Hubei, China, in 1963. She received a B.S. degree in Industrial Automation from the Wuhan University of Technology, Wuhan in 1984, an M.S. degree in Electrical Engineering from the Naval University of Engineering, Wuhan in 1987, and a Ph.D. degree in Electrical Engineering from the Huazhong University of Science and Technology (HUST), Wuhan in 2005. From 1987 to 1999, she was with the Department of Electrical Engineering, Naval University of Engineering, as a lecturer and associate professor. Since 1999, she has been with the College of Electrical and Electronic Engineering, HUST, where she became a full professor in 2005. In October 2010, she was a visiting scholar at the Center for Advanced Power Systems of Florida State University, Tallahassee. She has been engaged in research and teaching in the field of power electronics and electric drive. Her research interests include high-power high-performance AC motor drives, novel power converters, and their control. She has authored or coauthored more than 50 technical papers in journals and conferences. Dr. Lin was a recipient of the second-grade National Scientific and Technological Advance Prize of China in 1996 and 2003.